Journal of Materials Science & Technology 183 (2024) 63–71

Contents lists available at ScienceDirect

Journal of Materials Science & Technology

journal homepage: www.elsevier.com/locate/jmst

Research Article

# Origin of the high propensity for nanoscale deformation twins in CrCoNi medium-entropy alloy

Nan-Jun Liu[a,1], Zhang-Jie Wang[b,1], Jun Ding[b,*], Mark Asta[c,d], Robert O. Ritchie[c,d], Bin Gan[e], Evan Ma[b], Zhi-Wei Shan[a,*]

[a] Center for Advancing Materials Performance from the Nanoscale (CAMP-Nano), State Key Laboratory for Mechanical Behavior of Materials, Xi'an Jiaotong University, Xi'an 710049, China
[b] Center for Alloy Innovation and Design (CAID), State Key Laboratory for Mechanical Behavior of Materials, Xi'an Jiaotong University, Xi'an 710049, China
[c] Materials Sciences Division, Lawrence Berkeley National Laboratory, Berkeley, CA 94720, United States
[d] Department of Materials Science & Engineering, University of California, Berkeley, CA 94720, United States
[e] Beijing Key Laboratory of Advanced High Temperature Materials, Central Iron and Steel Research Institute, Beijing 100081, China

ARTICLE INFO

*Article history:*
Received 26 August 2023
Revised 27 September 2023
Accepted 3 October 2023
Available online 25 November 2023

*Keywords:*
High-entropy alloys
CrCoNi
Nanotwins
Twin nucleation

ABSTRACT

Single-phase face-centered cubic (fcc) high/medium-entropy alloys (H/MEAs) exhibit a much higher tendency to form nanoscale deformation twins than conventional fcc metals with similar low stacking fault energies (SFEs). This extraordinary propensity for nanotwin formation in H/MEAs cannot therefore be explained by their low SFEs alone. Here, using in situ compression tests of CrCoNi in comparison with Ag nanopillars inside a transmission electron microscope, we found that in the CrCoNi MEA, a high density of nanoscale twins continuously formed with an average thickness of 4.6 nm. In contrast, for similar experiments on Ag with almost identical SFE, following the nucleation of a few twins, they could further thicken to above one hundred nanometers by twin boundary migration. Molecular dynamics calculations indicated that in the highly-concentrated CrCoNi solid solution, the magnitude of the energy barriers for nucleating a stacking fault as a twin precursor in the pristine lattice and for the thickening of an existing twin both span a wide range and largely overlap with each other. Therefore, twin thickening through successive addition of atomic layers is prone to discontinuation, giving way to the nucleation of new twins at other sites where a lower energy barrier is encountered for partial-dislocation mediated fault formation.


## 1. Introduction

Face-centered cubic (fcc) high- or medium-entropy alloys (H/MEAs) with low stacking fault energies (SFEs) have been extensively studied in recent years, due to their excellent combination of strength, ductility and toughness at room and cryogenic temperatures [1–5]. Recent investigations of the underlying reasons examined the deformation mechanisms of these new alloys, including dislocation nucleation and slip, deformation twinning, and phase transformation [6–15].

Deformation twinning is a common mechanism of plastic deformation that is well understood in traditional fcc metals and alloys [16–19]. However, in H/MEAs, the motion of the partial dislocations, which mediate deformation twinning, is influenced by inherent local composition fluctuation as well as chemical short-range ordering in the H/MEAs [15,20-24]. Moreover, unconventional phase transformation-assisted twinning was reported in HEAs [11,25,26], which made it possible to form complex structures such as twin-hcp laminated substructures. In this work, we illustrate another example of unusual twinning behavior in HEA/MEAs, focusing on the nucleation of new twins in competition with the thickening of existing ones, to uncover the origin for the observation of profuse nanoscale deformation twins which contribute to high strength and ductility [2,3,5,6,14,27-30], specifically in the equiatomic CrCoNi alloy.

In conventional fcc metals, a Shockley partial dislocation can readily move on an existing twin boundary as it only encounters a low energy barrier [16,31]. By comparison, the nucleation of a leading partial dislocation in the pristine lattice is more difficult, as it is required to overcome a sizable activation energy due to the creation of a new stacking fault (SF). The implication of this is that, with imposed plastic strain, existing twins have a larger tendency to widen rather than nucleate new SFs and twins elsewhere in the crystal. Indeed, in metals with relatively low stack-

* Corresponding authors.
*E-mail addresses:* dingsn@xjtu.edu.cn (J. Ding), zwshan@xjtu.edu.cn (Z.-W. Shan).
[1] These authors contributed equally to this work.

https://doi.org/10.1016/j.jmst.2023.10.025
1005-0302/

ing fault energies (SFEs), such as gold with SFE of 33 mJ/m$^2$, uniaxial tension tests on defect-free nanowires have shown that deformation twinning contributes to most of the plastic strain and that the twin lamellae widen to as thick as 1 $\mu$m via a mechanism of progressive layer-by-layer migration of the twin boundaries [32–34]. A similar twin propagation process has also been observed in Cu, Pd, and Ag nanowires [35–37]. As we discuss below, a multiple-principal-element alloy with low SFE defies this norm. Observations are that very narrow twins, typically only a few nanometers in thickness, are more prevalent in deformed low-SFE H/MEAs, such as in CrCoNi [2,3,27,29,30,38–40], CrMnFeCoNi [1,41–44], Al0.1CrFeCoNi [45], and Cr20Mn20Fe20Co15Ni25 [46]. Previous studies simply attributed this clear tendency for a predominant number of nanometer-thick twins to form in these non-dilute solid-solution alloys to their low SFEs [29,39,46]. However, as will be discussed later, even traditional fcc metals with almost identical low SFEs do not necessarily exhibit such profuse nanoscale deformation twins. This suggests that there must be other important, unrecognized factors other than low SFEs at work.

In this paper, we provide insight into the origin of the different deformation twinning behavior in H/MEAs. We note that these alloys, as highly concentrated solid solutions, engender an additional variable that the atomic arrangement on each slip plane is substantially different. As a result, the atomic packing as well as the chemical environment that the twinning (partial) dislocation is subjected to will vary from one atomic plane to another. As the corresponding varying degrees of difficulty for the moving Shockley partial dislocations could span a wide range, the mechanism of twin thickening by boundary migration is likely to be periodically disfavored after it occurs over a few atomic planes. Instead of widening the already-formed twins, stacking faults emerge elsewhere, leading to frequent twin nucleation at new sites.

To demonstrate that this hypothesis is conceptually correct, we examined the deformation twinning behavior of the single-phase equiatomic CrCoNi alloy as a model H/MEA to contrast directly with Ag as a representative traditional fcc metal. These two fcc structures have similarly low SFEs, ~22 ± 4 mJ/m$^2$ for CrCoNi [2] and ~21 mJ/m$^2$ for Ag [16], and both are prone to deformation twinning during plastic deformation at room temperature [2,6,30]. We tested these two materials using in situ compression experiments in the transmission electron microscope (TEM) using similar sample sizes and loading orientations to observe the mechanistic details of twin formation and propagation. Significant differences in the deformation twinning behavior in CrCoNi and Ag were seen. The continuous nucleation of a high density of dispersed nanoscale twins (with an average thickness of 4.6 nm) mediates plastic deformation in CrCoNi, whereas in stark contrast, the continuous thickening of a few twins by twin boundary migration defined the corresponding deformation behavior in Ag. To understand the origin of these observations, we used molecular dynamics (MD) simulations and modeling to demonstrate the contrasting deformation twinning behavior between CrCoNi and Ag. We revealed that the locally varying atomic arrangement in CrCoNi MEA broadens the distributions of the energy barriers for twin nucleation and thickening, which causes a transition from mechanisms involving the thickening of existing twins in conventional fcc metals, to one involving the continuous formation of new twins, each having nanometer-width.

## 2. Experimental

### 2.1. Sample preparation

Our samples were single crystals to avoid the influence of grain boundaries and facilitate the definition of a required loading orientation. Equiatomic CrCoNi single crystals were grown by the Bridgman method using pure metals (>99.9 wt.%) in an argon atmosphere. Ag single crystals (99.999% pure) were purchased from GoodFellow Corporation (Shanghai, China). The CrCoNi ingot was homogenized at 1200 °C for 24 h and then water-quenched to room temperature (RT). The axial direction of single crystals of both CrCoNi and Ag is [010], characterized by electron backscatter diffraction (EBSD). Both single-crystal ingots of CrCoNi and Ag were electrical-discharge cut into small slices with dimensions of ~2 mm × 2 mm × 1 mm and mechanically thinned down to a thickness of ~50 $\mu$m, followed by electrochemical polishing in a solution of $HClO_4$:$C_2H_6O$=1:10 at room temperature with a voltage of 15 V. From the thin areas of the wedged slice, we fabricated pillars of both CrCoNi and Ag with diameters smaller than 300 nm and with a height-to-diameter ratio of ~2.5:1 to ~3.5:1 using a focused ion beam (FIB, FEI Helios NanoLab 600 dual-beam systems). During this step, the beam current was gradually decreased from 21 nA to 28 pA while the accelerating voltage of the ion beam was kept at 30 kV. We designed the diameter of pillars considering size-dependent propensity of deformation twinning in micropillars at room temperature. Tension of nanowires of fcc metals already revealed that below a critical diameter deformation twinning mediated the plasticity while above this size dislocations slip contributed to most of the plasticity [47]. Compression of CrCoNi micropillars along [001] orientation with diameters in the range of 3 $\mu$m to 100 nm exhibited that twinning mediated plasticity in the pillars with diameters smaller than 300 nm. Thus, we focused on these pillars (diameter < 300 nm) for the purpose of observing the twin nucleation and thickening.

### 2.2. In situ compression tests inside TEM

Further compression tests in displacement control mode were carried out in the TEM (JEOL JEM 2100F) at 200 kV using a Hysitron TEM Picoindenter (PI95). The loading process was captured by a Gatan 833 (SC200D) CCD camera at a rate of 10 frames per second. The strain rate was set at $10^{-2}$ s$^{-1}$, with the maximum engineering strain limited to ~20%. To observe the twin formation, all the compression tests were performed with the loading direction aligned along the ⟨010⟩ twinning orientation to guarantee a larger Schmid factor for the leading partial dislocations [48]. The incident electron beam was along ⟨101⟩ to clearly observe the twins on the edge-on {111} planes.

### 2.3. Molecular dynamics (MD) simulations of deformation twinning behavior

MD simulations were implemented to examine deformation twinning behavior of the CrCoNi alloy and Ag using empirical Embedded-Atom-Method (EAM) potentials [49,50] by applying two kinds of deformation modes, namely shear and uniaxial compression. For the CrCoNi alloy, hybrid MD and Monte Carlo simulations were carried out, under the variance-constrained semi-grand-canonical ensemble, to obtain the equilibrium configurations at the annealing temperature of 1000 K, which has been demonstrated to give rise to a degree of chemical short-range order [50]. For shear deformation, the samples had dimensions of ~10.8 nm in *x*, 10 nm in *y*, and 30 nm in *z*, each containing 288,000 atoms (*x*, *y* and *z* are orthogonal directions). Periodic boundary conditions were imposed along the *x*- and *y*-directions with a shrink-wrapped non-periodic boundary condition in the *z*-direction. During the loading step, the bottom two layers of atoms in the *z*-direction were fixed, and the top two layers of atoms were treated as a rigid body, while the Canonical NVT ensemble was applied to other atoms. For compression, nanopillar samples with a diameter of 20 nm and length of ~80 nm were prepared with all three dimensions as the free

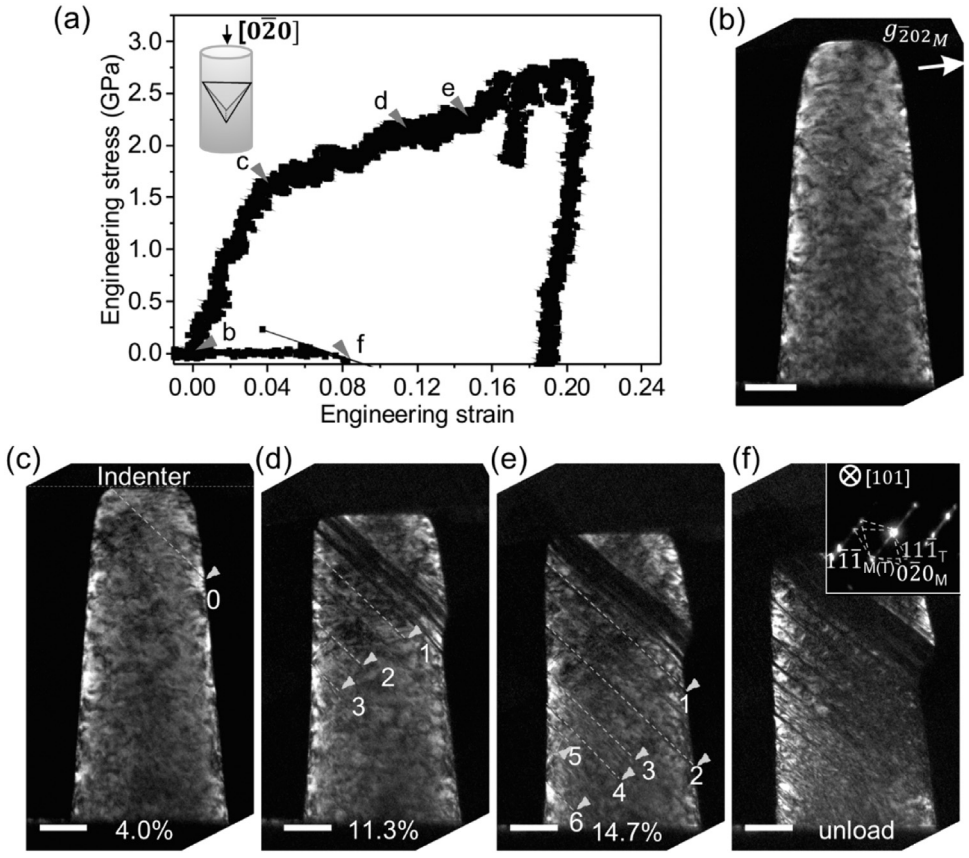


**Fig. 1.** Deformation behavior of a CrCoNi pillar with a diameter $D$ = 105 nm during compression along [0$\bar{2}$0]. (a) Engineering compressive strain-stress curve and dark-field images using $\boldsymbol{g} = \bar{2}02_M$ extracted from the in situ Movie S1 (b) prior to loading, (c) at the apparent yielding point corresponding to the formation of the first twin (twin 0) from the contact interface with the indenter, (d) when twins (twin 1, 2, 3) nucleate from the free surface that is not in contact with the indenter and propagate into the interior of the pillar, (e) at the point of nucleation of the new twins 4, 5, 6 when twin 3 is still resident in the pillar, and (f) after unloading. The diffraction pattern in (f) shows extra spots for twins (yellow), symmetrical to the matrix spots (white) about the plane (1$\bar{1}\bar{1}$). Scale bars, 50 nm.

surface. Prior to deformation, a pre-existing nanotwin of 15 layers (~3 nm) was first introduced in the middle of both the CrCoNi and Ag samples. An applied strain rate of 5 × $10^6$ $s^{-1}$ was used in all simulations.

### 2.4. Methods for calculation of the generalized stacking fault energies in CrCoNi and Ag

We employed nudged-elastic-band (NEB) method to investigate the generalized stacking fault energy surfaces in CrCoNi and Ag. During the NEB simulation, the atoms are relaxed to the minimum energy paths. The NEB method is more accurate in calculating the energy barriers than the more conventional approach of rigidly shifting the atoms along a slip plane for M/HEAs, considering their intrinsic lattice distortion. An intrinsic SF is introduced by shearing a {111} plane along the ⟨112⟩ direction, which undergoes structural relaxation for energy barrier calculation. To construct the twinning configuration, a neighboring {111} plane of the intrinsic SF is continuously sheared in the same ⟨112⟩ direction and relaxed. Another shearing of {111} plane, results in twin thickening from two layers to three layers. Detailed descriptions and schematics can be seen in Section 3.5. $\gamma_{isf}$ and $\gamma_{esf}$ represent the stacking fault energies of an intrinsic SF and extrinsic SF. $\gamma_{usf}$ and $\gamma_{utf}$ are the unstable stacking fault energy and unstable twinning fault energy. We focus on three energy barriers $\gamma_{usf}$, $\gamma_{ut-1}$ and $\gamma_{ut-2}$, for SF nucleation, twin formation, and twin thickening, respectively.

## 3. Results and discussion

### 3.1. In situ compression of CrCoNi nanopillars

Fig. 1 shows the compression testing results for a CrCoNi pillar with a diameter $D$ = 105 nm and a taper of ~4°. The engineering strain-stress curve (the engineering stress is calculated as the ratio of the load to the cross-section area at the top of the pillar), shown in Fig. 1(a), is rather continuous and smooth, without the well-known intermittent flow characterized by pronounced strain bursts in micro- and nanosized single-crystal pillar compression curves in metals [51–53]. Fig. 1(b-f) shows the frames extracted from the recorded Movie S1 in Supplementary Information that corresponds to marked points b-f in the strain-stress curve. All the frames are dark-field images using the diffraction vector $\boldsymbol{g} = \bar{2}02_M$ from the [101] viewing direction; the subscripts M or T here represent that these diffraction vectors belong to the matrix or the twin. The as-fabricated pillar with FIB-introduced defects and pre-existing dislocations can be seen in Fig. 1(b). The first twin (twin 0 in Fig. 1(c)) was emitted from the contact interface between the indenter and pillar at an engineering strain of 4.0%, corresponding to the apparent yield point c in Fig. 1(a). It was followed by the continuous formation of nanoscale twins at the contact interface (Movie S1). Above a strain of ~7.4%, twins began to nucleate from the free surface. For example, we observed three twins (twin 1, 2 and 3) in Fig. 1(d), nucleating from the free surface at strains of 10.8% (twin 1 and 2) and 11.3% (twin 3). These twins

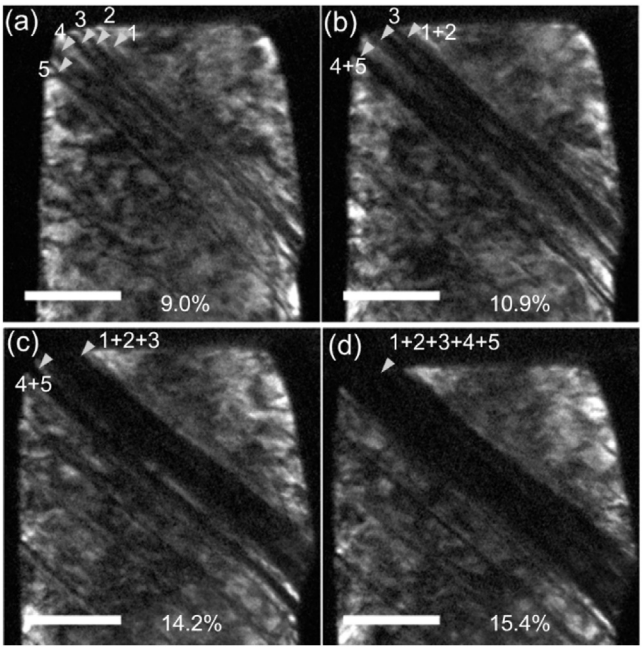


**Fig. 2.** Merging progress of twins. (a) Five separate twins with a thickness of ~3 nm nucleating at the top of the pillar. (b) Twins 1 and 2 merge into 1 + 2, and twins 4 and 5 merge into twin 4 + 5 at an increased strain of 10.9%, by a new twin nucleating in the matrix between them. (c, d) A similar merging process finally resulting in twin 1 + 2 + 3 + 4 + 5 with a thickness of 32 nm. Scale bars, 50 nm.

did not traverse the pillar immediately; rather it took a time of 1.1 s for twin 1 and 2.8 s for twin 2 to run through the pillar at strains of 12.2% and 14.1%, respectively. For twin 3 in Fig. 1(e), its leading edge was still resident in the pillar even after new twins (twin 4–6) nucleated. This slow lengthening of the twins in the CrCoNi alloy is in sharp contrast with the scenario in conventional fcc metals, where the front end of a twin generally runs from one boundary (e.g., a surface of the microsample or a grain boundary) to another boundary immediately after its nucleation [33,36,37]; this will also be the case for Ag, the representative low-SFE metal we used for comparison. Moreover, the nucleation of twins in the MEA occurred uniformly from the surface along the entire pillar. These twins maintained their initial small thickness after formation, which resulted in a high density of nanometer-thick twins, as clearly shown in the compressed pillar after unloading (Fig. 1(f)). The exception was one ~32 nm thick lamella in the contact area, where in situ TEM observations clearly revealed that it achieved its final large thickness by merging thin lamellae when a new twin nucleated between two existing lamellae.

Fig. 2 shows enlarged TEM images of the merging process of the in-contact twins shown in Fig. 1. First, five separate twins (twin 1, 2, 3, 4, and 5) with thicknesses of ~3 nm nucleated at the top of the pillar (Fig. 2(a)). At a strain of 10.9%, twin 4 and 5 merged into twin 4 + 5 via the creation of a new twin formed in the matrix in between them. Twin 1 and 2 similarly merged into twin 1 + 2; with increasing strain, additional new twin nucleation occurred between twin 1 + 2 and twin 3 that then merged into twin 1 + 2 + 3 (Fig. 2(c)). Finally, the merging of twin 1 + 2 + 3 with

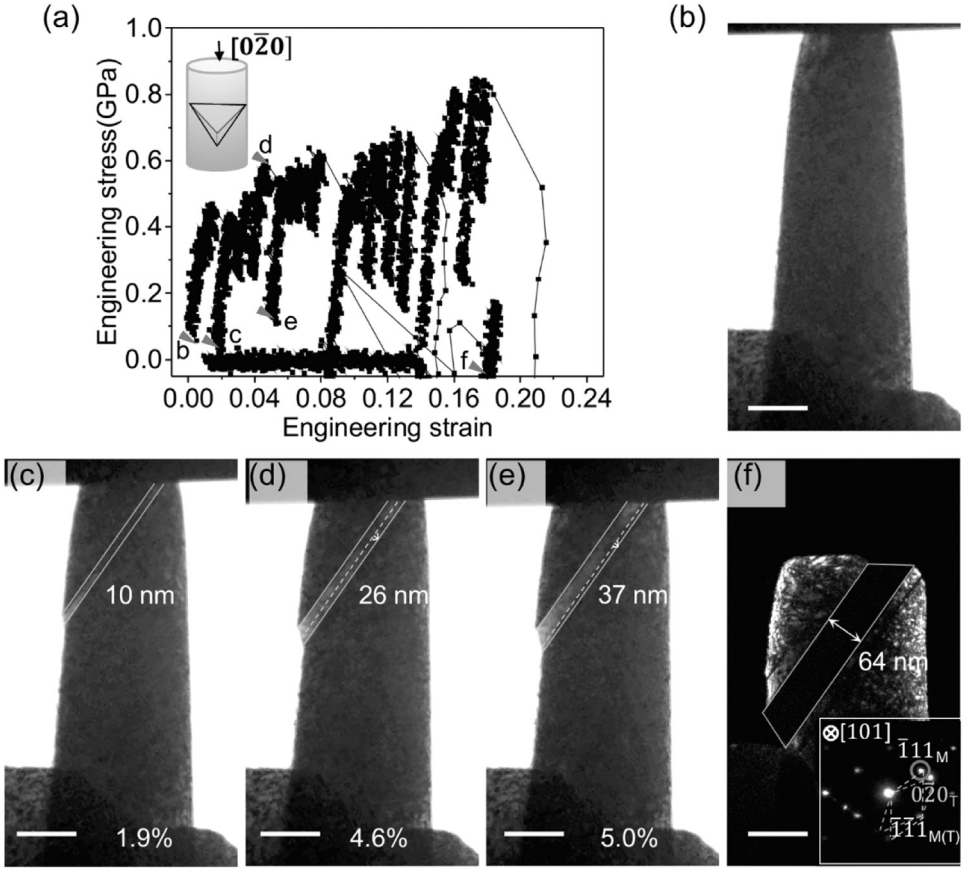


**Fig. 3.** Deformation behavior of a $D$ = 167 nm Ag pillar during compression along [0$\bar{2}$0]. (a) Engineering compressive strain-stress curve and in situ TEM bright-field images (b) before loading, (c) after the first burst related to the formation of a 10-nm thick twin, (d) during twin thickening to 26 nm by twin boundary migration, (e) after another burst related to the thickening of the twin. (f) Postmortem dark-field image using **g**=$\bar{1}11_M$ showing a 64 nm-thick twin. Scale bars, 100 nm.

twin 4 + 5 resulted in a final thick twin with a thickness of 32 nm (Fig. 2(d)).

This merging and thickening mechanism has also been observed by in situ high-resolution TEM straining in Al0.1CrFeCoNi [54]. It can also be seen in severely deformed macro-scale high entropy alloys, where some of the "thick twins", observed in TEM at low magnifications [42,44], actually comprised many thin lamellae formed into a bundle when imaged at high magnification [43,44]. This process is quite distinct from the well-reported twin thickening mechanism by twin boundary migration [33].

### 3.2. In situ compression of Ag nanopillars

As noted earlier, deformation twinning behavior in Ag is totally different. Fig. 3 and Movie S2 show the deformation process in one Ag pillar (with $D = 167$ nm and a taper of ~4°). The corresponding compressive engineering strain-stress curve (Fig. 3(a)) is quite distinct from the smooth curve observed for CrCoNi (Fig. 1(a)), with pronounced strain bursts. Fig. 3(b) shows the pillar before loading also with many pre-existing dislocations and defects caused by FIB damages. The pillar just after the first burst (c point in Fig. 3(a)) shows twin formation and subsequent quick propagation through the pillar with thickening to 10 nm (Fig. 3(c)), a process that took less than 0.1 s (measured by the time interval between the two frames in Movie S2). The twin thickened to 26 nm (Fig. 3(d)) by twin boundary migration along the direction of the arrow from point c to d in Fig. 3(a). A burst occurred at point d, accompanied by twin thickening to 37 nm immediately, as shown in Fig. 3(e). After compression to a maximum strain of 21.5%, the twin lamella grew to a thickness of 64 nm (Fig. 3(f)). Instead of merging thin twin lamellae as was seen in CrCoNi, twin thickening by twin boundary migration was clearly observed in Ag in the dark-field images in Fig. S1 and Movie S2 in Supplementary Information. Additionally, with the exception of the thick twins at the contact interface, the nucleation of twins at the free surface was rarely observed. High stress concentration at the corners of the thick twin lamella in Ag may promote subsequent thickening of the existing twin. However, considering that stress concentration also existed in CrCoNi pillars at the corner of twins (such as the thick twin near the contact interface at an engineering strain of 14.7%, shown in Fig. 1(e)), and yet new nanotwins still nucleated at the free surface, the different twinning behaviors in the two materials should be governed by intrinsic factors, rather than stress concentration.

### 3.3. Statistic results of twins in CrCoNi and Ag nanopillars

The number and thickness of twins in the six pillars for Ag and CrCoNi were summarized in Fig. 4, without distinguishing the nucleation sites (from the contact interface or the free surface). For CrCoNi, a large number of twins formed, specifically a total of 100 in six pillars. Most of these twins had a small (< 10 nm) thickness, primarily in the 4 nm to 6 nm range, with an average thickness of only 4.6 nm (fitted by the Gaussian distribution shown in red in Fig. 4(a)). In contrast, a much smaller number of twins formed in Ag—a total of only 14 twins in six pillars. These twins generally had a much larger thickness (up to 131 nm, see Fig. 4(b)), all of which were generated at the contact interface. In addition to their differing size, the mechanism of thickening of the twins was also completely different in CrCoNi and Ag: twins thickened by the merging of thin lamellae in CrCoNi (the inset schematics in Fig. 4(a)) while by twin boundary migration in Ag (the inset schematics in Fig. 4(b)), respectively.

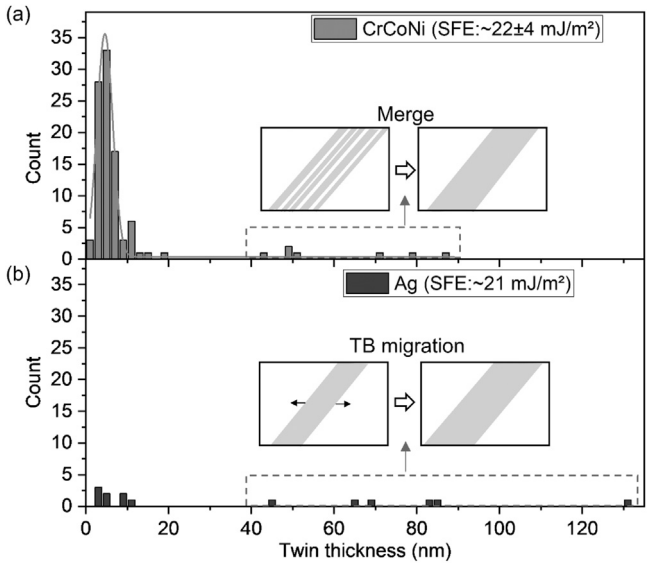


**Fig. 4.** Twins thickness distribution in CrCoNi and Ag. Twins in six pillars for each material were summarized, without distinguishing the nucleation sites (from the contact interface or the free surface). (a) For CrCoNi, a large number of twins formed. The red line is the Gaussian fitting curve, with an average thickness of 4.6 nm. Thickened twins were created by merging thin lamellae, as shown in the inset schematic. (b) Few twins were formed in Ag, generally with a larger thickness; these thickened by the process of twin boundary migration.

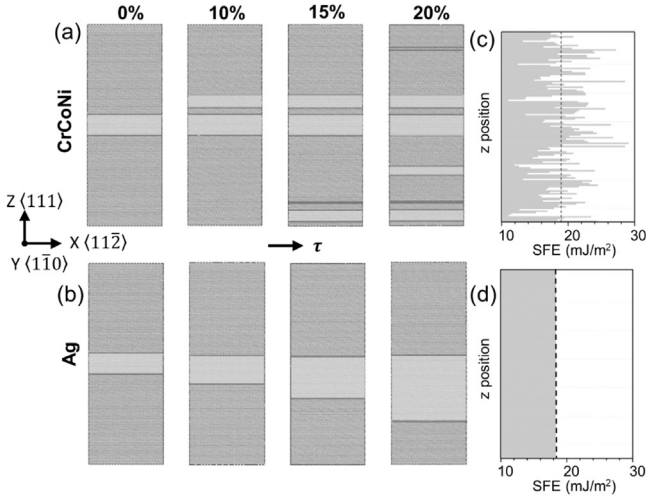


**Fig. 5.** MD simulation of deformation twinning in the CrCoNi alloy and Ag. For (a) CrCoNi alloy and (b) Ag, a pre-existing nanotwin (consisting of 15 layers) was first introduced into the initial configuration, which was subjected to shear deformation up to a strain of 20%. The atoms are colored according to common neighbor analysis: blue, red, and white atoms represent fcc, hcp and other structures, respectively. Nanotwins are indicated by yellow shades. The *x*, *y* and *z* directions are for ⟨11$\bar{2}$⟩, ⟨1$\bar{1}$0⟩ and ⟨111⟩, respectively. The calculated SFEs of planes along the *z*-direction are shown for the (c) CrCoNi alloy and (d) Ag. Only {111} planes away from free surfaces (top and bottom layers along the *z*-axis) by > 1 nm are plotted. The dashed lines indicate the average value of the SFE. .

### 3.4. Molecular dynamics simulation of deformation twinning process

Similar difference in deformation twinning behavior in CrCoNi and Ag was also observed in MD simulations. Details of the simulation procedures are documented in the Section 2.3. Specifically, a pre-existing nanotwin of 15 layers was first introduced into the middle of samples of both the CrCoNi alloy and Ag; the samples were then subjected to shear loading up to a strain of 20%. The respective atomic configurations are shown in Fig. 5(a) and (b). Nanotwins are indicated by yellow shades. First considering the CrCoNi

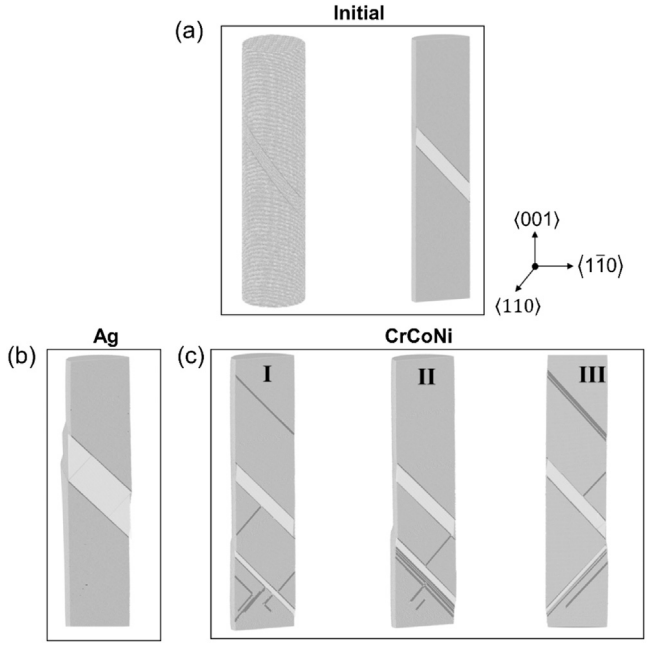


**Fig. 6.** MD simulation of the compression deformation of the CrCoNi alloy and silver, both with a pre-existing nanotwin. (a) Initial configuration of a nanopillar with a diameter of 20 nm and length of ~80 nm; a nanotwin with a thickness of ~ 3 nm was introduced; all three dimensions are set at the free surface; the atoms are colored according to common neighbor analysis: blue, red and white atoms represent fcc, hcp and other structures, respectively; the nanotwins are indicated by yellow shades. (b) Atomic configuration of Ag after a compressive strain of 4%. (c) Three independent cases (denoted as I, II and III) of the CrCoNi alloy after a compressive strain of 4%. Compression was applied for both the Ag and CrCoNi alloys at strain rates of $5 \times 10^6$ $s^{-1}$ at 300 K.

MEA in Fig. 5(a), the increasing shear strain generated three new nanotwins, along with intrinsic and extrinsic stacking faults, with no evidence of broadening of the pre-existing nanotwin. In contrast, the Ag sample underwent immediate thickening of the pre-existing nanotwins (Fig. 5(b)).

Simulations over larger dimensions for the uniaxial compression of nanopillars, gave essentially identical results (see Fig. 6). Fig. 6(a) shows the initial configuration of nanopillar with a diameter of 20 nm and length of ~80 nm, containing a single nanotwin of thickness ~3 nm. The atomic configuration of Ag after a compressive strain of 4%, shown in Fig. 6(b), indicates that only the preexisting twin thickened, without any nucleation of new twins. Fig. 6(c) shows three independent cases (denoted as I, II and III) for the CrCoNi alloy after a compressive strain of 4%. In all three cases, numerous new twins and SFs nucleated, twins from different twinning systems leading to the intersection of twins in different directions.

Since the average SFE is similar in Ag and CrCoNi (Fig. 5(c, d)), it is obviously unreasonable to explain the twinning behavior difference from the perspective of just the low SFE alone.

### 3.5. Generalized stacking fault energies in CrCoNi and Ag

To unveil the intrinsic mechanism for the nanoscale twins in CrCoNi, we employed NEB method to investigate the generalized stacking fault energy surfaces, as illustrated in Fig. 7(a–e). For a twin nucleation in the pristine lattice, the very first step is to nucleate an intrinsic SF, with $\gamma_{usf}$ to overcome. Further extending layers of SF will encounter energy barriers $\gamma_{ut-1}$ and $\gamma_{ut-2}$ (see Fig. 7(e)), resulting in twin formation and further twin thickening. For elemental metals and conventional alloys, there usually exists such a relationship: $\gamma_{usf} > \gamma_{ut-1} = \gamma_{ut-2}$ . For Ag here, $\gamma_{usf} = 114.4$ mJ/m$^2$, $\gamma_{ut-1} = 98.9$ mJ/m$^2$ and $\gamma_{ut-2} = 98.9$ mJ/m$^2$, as shown in the inset illustration in Fig. 7(f). In this case, it is easier for the thickening of an existing SF or twin, when compared to nucleating a new SF in the pristine lattice of Ag. In contrast, for a CrCoNi alloy, Fig. 7(f) shows the distribution of calculated results of $\gamma_{usf}$, $\gamma_{ut-1}$ and $\gamma_{ut-2}$ in a total number of 100 independent samples, where those three barriers exhibit very wide distributions and they are also largely overlapped. Besides, the average values of $\gamma_{usf}$, $\gamma_{ut-1}$ and $\gamma_{ut-2}$ are nearly identical (256 mJ/m$^2$ vs 255 mJ/m$^2$ vs 255 mJ/m$^2$). Such widely distributed energy barriers, nearly equal in average magnitude, enable the concurrent activation of twin nucleation and propagation. To illustrate why this would result in a high propensity for nanoscale deformation twins in the CrCoNi alloys, let us consider a twin lamella that attempts to thicken to tens of nanometers. For this to be accomplished, successive shearing of neighboring {111} planes with low energy barrier must happen above one hundred times. Such a chance would be extremely low, considering the significantly varied energy barriers for twin thickening on different atomic planes. Once a plane with a higher energy barrier is encountered thickening would stop and the strain would be carried by an SF (nucleating a new twin) elsewhere at a new site with a lower $\gamma_{usf}$. Thus, a high density of nanoscale twins, instead of individual thick twins, prefer to form in the CrCoNi alloy. This explains the experimental observation during our in-situ nanoscale deformation and large-scale MD simulation.

We also clarify what specific atomic configurations (i.e., local chemical environment) are the most preferable versus undesirable nucleation sites for twins in CrCoNi, which has been shown above to exhibit a wide distribution of energy barriers in Fig. 7(f). Here the local chemical environment is variable in terms of not only compositional fluctuation [55] but also chemical short-range order (CSRO) [12]. As shown in Fig. 7(g), the independent CrCoNi configurations are grouped according to their magnitude of $\gamma_{usf}$; the corresponding average fraction of elements (Left axis in Fig. 7(f)) and the average Warren-Cowley parameter of Co-Cr pairs (Right axis in Fig. 7(f)) located at the SFs are analyzed. The obtained results are bifurcated: On one hand, the higher the fraction of Ni atoms (or less fraction of Co and Cr atoms), the larger the energy barrier of $\gamma_{usf}$. On the other hand, with the increasing $\gamma_{usf}$, the Warren-Cowley parameter of Co-Cr pairs, as the characteristic CSRO feature for CrCoNi alloys [8], becomes increasingly negative, indicating the favored Co-Cr paring (Negative (Positive) values of Warren-Cowley parameter correspond to a tendency of favored (unfavored) pairs). Therefore, atomic planes with less fraction of Ni atoms, or less preference of Co-Cr pairs, corresponding to lower $\gamma_{usf}$, are prone to nucleate SFs or twins, and vice versa. This is the structural origin of the highly inhomogeneous and largely overlapped energy barriers involved in the twinning process.

### 3.6. Contribution of high propensity for twin nucleation to mechanical properties in CrCoNi

High preference for twin nucleation at new sites can contribute to strain hardening and high strength in fcc H/MEAs, which represents an important contribution to the strength, ductility, and toughness of these alloys [1–3,42]. Our observations in severely deformed pillars clearly demonstrate that a high density of intersecting twins can form due to abundant nucleation sites, resulting in strain hardening.

Fig. 8 shows such an example in a $D = 90$ nm CrCoNi pillar (also see Movie S3). At small strains, the deformation process was similar to that described above; separate nanoscale twins on a twin plane $(\bar{1}11)$ nucleated from the contact interface and merged into thicker twins, as shown in Fig. 8(b–d) (the twins appear dark under $\boldsymbol{g} = 20\bar{2}_M$). However, at a large strain of 13.6%, the twins on another new plane $(\bar{1}\bar{1}1)$ became activated (Fig. 8(d)); in one ex-

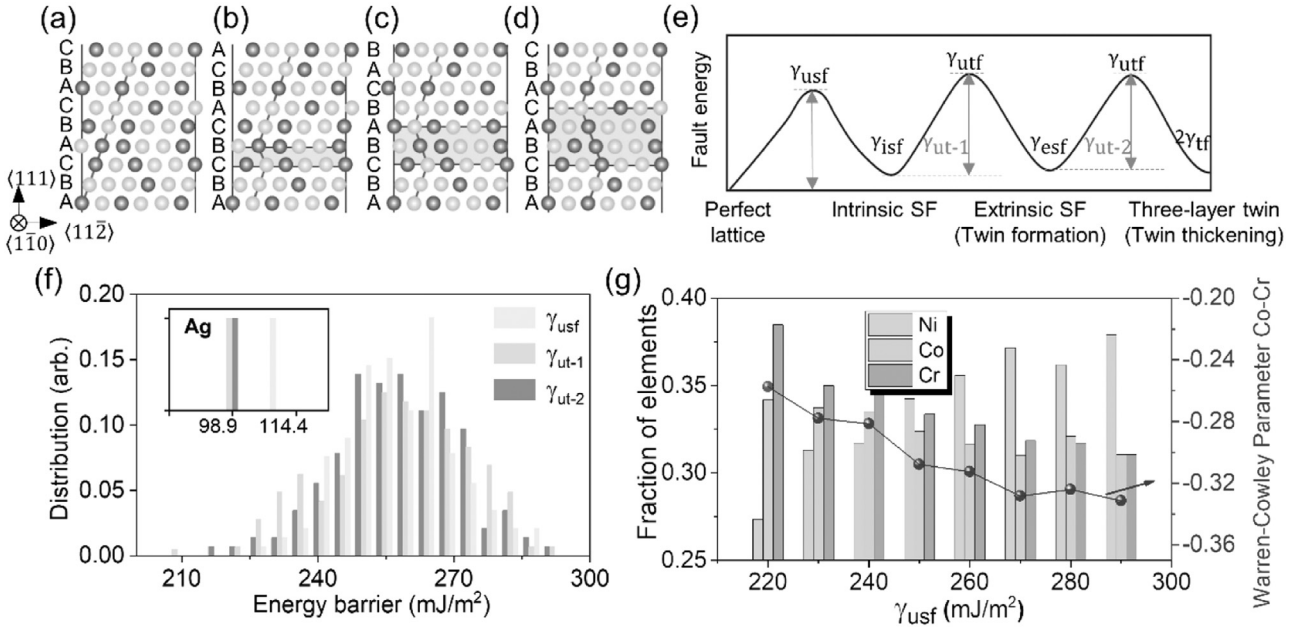


**Fig. 7.** Distribution of energy barriers for twinning process. (a–d) Atomic configuration of perfect lattice, intrinsic stacking fault, extrinsic stacking fault and a three-layer twin, respectively. (e) Energy barriers along the ⟨11$\bar{2}$⟩ direction displacement which results in the stacking fault, twin formation, and twin thickening. (f) Distribution of calculated unstable stacking fault energy $\gamma_{usf}$ and the energy barrier for twin formation ($\gamma_{ut-1}$) and twin thickening ($\gamma_{ut-2}$) in CrCoNi alloy by the NEB method. A total number of 100 independent samples were studied and the size of SF is about 2 nm. The inset illustration shows the same calculated data for Ag. (g) Average fraction of elements (Left axis) and the average Warren-Cowley parameter of Co-Cr pairs (Right axis), located at the SFs for a variety of groups of $\gamma_{usf}$ in the CrCoNi alloy.

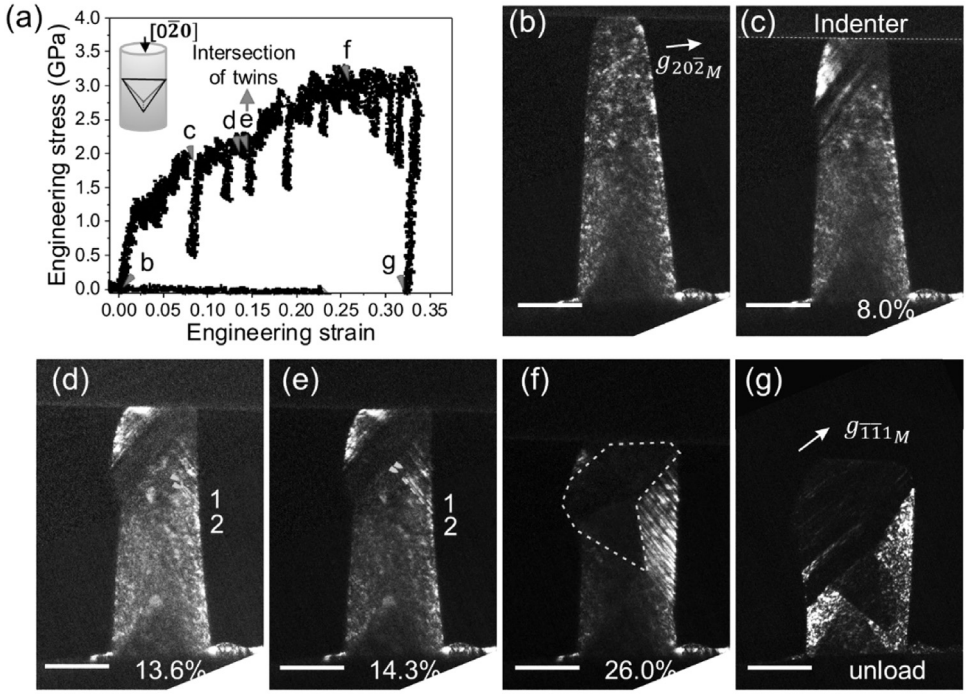


**Fig. 8.** Deformation behavior of a $D = 90$ nm CrCoNi pillar with multiple twinning systems. (a) Engineering compressive strain-stress curve and dark-field TEM images using $\boldsymbol{g} = 20\bar{2}_M$ extracted from the in situ movie at the moment of (b) before loading, (c) separate twins with twin plane ($\bar{1}11$) nucleating at the contact surface, (d) existing twins merging, and twins 1 and 2 with a new twin plane ($\bar{1}\bar{1}1$) nucleating at the free surface, (e) twins 1 and 2 propagating forward, the intersection of the twins inducing an increase in the engineering stress, and (f) formation of a high density of twins with an average twin spacing of 3.3 nm. (g) Postmortem dark-field image using $\boldsymbol{g} = \bar{1}\bar{1}1$ M showing the residual matrix in twins of twin plane ($\bar{1}11$) with tortuous boundaries. Scale bars, 100 nm. The twins shown here were not included in the twin thickness distribution shown in Fig. 4.

ample, twin 1 and 2 nucleated from the free surface, and further propagated toward the opposite surface (Fig. 8(e)). Subsequently, copious nanoscale twins can be seen to have continuously nucleated. The intersection of such multi-orientation twins leads to an obvious increase in engineering stress after point e. Indeed, an extremely high-density twin, with an average twin spacing of 3.3 nm, can be observed in Fig. 8(f) at a larger strain of 26.0%. Twins from two different planes appear dark in Fig. 8(b–f) using a diffraction vector $\boldsymbol{g} = \bar{2}02_M$. In Fig. 8(g), we used another diffraction vector $\boldsymbol{g} = \bar{1}\bar{1}1$ M with a stronger diffraction density to obtain a centered dark-field image. This image shows that the entire wide dark band (marked in Fig. 8(f) by yellow dashed lines) actually contains

a nanoscale matrix (bright) with separate twins (dark) with tortuous boundaries; this is an example of the incomplete merging of thin lamellae.

Such intersecting twins are directly observed here for the first time in such a small volume and have been rarely reported in traditional fcc nanopillars or nanowires, such as Au, Ag and Cu [33,37,56,57].

## 4. Conclusion

In summary, these findings highlight a new consequence of the distinctly different structural features of H/MEAs, which despite their simple crystal structures are highly concentrated solid solutions characterized by local inhomogeneity. A key difference from normal low-SFE fcc metals therefore arises in that the local energy barriers encountered by the glide of twinning partial dislocations vary, not only over a wide range but also from location to location. While the spatially varying SFE has been noted [58–63], our new point is that the overlap in barrier heights induces a twinning behavior quite different from conventional metals. Specifically, we observe, and can explain using simulations/calculations, a high propensity for the emergence of new twins in H/MEAs, in lieu of the continued widening of existing twins to tens of nanometers in thickness expected in conventional low-SFE fcc metals. While the differences in twinning behavior revealed here for CrCoNi and Ag were observed in single-crystal micropillars, we believe that these differences would still exist in more widely available polycrystalline materials. One example is that after deformation of polycrystalline samples at liquid nitrogen temperature, a smaller average twin thickness (~8 nm) was also seen in deformed CrCoNi [46] than in Ag (50–60 nm) [64]. However, we note that a systematic comparison of twin nucleation and propagation behavior between polycrystalline CrCoNi and Ag requires strict control of the grain size, type of grain boundaries, loading conditions, etc. In general, grain boundaries would provide more potent nucleation sites for deformation twins, compared with the surface as the nucleation source here.

## Declaration of Competing Interest

The authors declare that they have no known competing financial interests or personal relationships that could have appeared to influence the work reported in this paper.

## Acknowledgments

This work was financially supported by the National Natural Science Foundation of China (Nos. 52231001, 51971167, and 52031011) and the Xi'an Science and Technology Plan (No. 2017xasjl014). B.G. gratefully acknowledges the financial support of the project from the Ministry of Science and Technology of China (No. 2017YFA0700703) and the support by the National Natural Science Foundation of China (No. 92060102). E.M. and J.D. acknowledge the support at CAID by XJTU. J.D. acknowledges support from the National Natural Science Foundation of China (No. 12004294) and the HPC platform of Xi'an Jiaotong University. M.A. and R.O.R. were supported by the Office of Science, Office of Basic Energy Sciences, Materials Sciences and Engineering Division, of the U.S. Department of Energy under Contract No. DE-AC02–05-CH11231. FIB fabrication and in-situ TEM compression were carried out at the Center for Advancing Materials Performance from the Nanoscale (CAMP-Nano). We thank Peng Zhang at CAMP-Nano for his help in using TEM.

## Supplementary materials

Supplementary material associated with this article can be found, in the online version, at doi:10.1016/j.jmst.2023.10.025.

## References

[1] A.Hohenwarter B.Gludovatz, D. Catoor, E.H. Chang, E.P. George, R.O. Ritchie, Science 345 (2014) 1153–1158.
[2] G. Laplanche, A. Kostka, C. Reinhart, J. Hunfeld, G. Eggeler, E.P. George, Acta Mater. 128 (2017) 292–303.
[3] B. Gludovatz, A. Hohenwarter, K.V. Thurston, H. Bei, Z. Wu, E.P. George, R.O. Ritchie, Nat. Commun. 7 (2016) 10602.
[4] X.H. Du, W.P. Li, H.T. Chang, T. Yang, G.S. Duan, B.L. Wu, J.C. Huang, F.R. Chen, C.T. Liu, W.S. Chuang, Y. Lu, M.L. Sui, E.W. Huang, Nat. Commun. 11 (2020) 2390.
[5] P. Gao, S. Sun, H. Li, R. Niu, S. Han, H. Zong, H. Wang, J. Lian, X. Liao, J. Mater. Sci. Technol. 106 (2022) 1–9.
[6] Z. Zhang, H. Sheng, Z. Wang, B. Gludovatz, Z. Zhang, E.P. George, Q. Yu, S.X. Mao, R.O. Ritchie, Nat. Commun. 8 (2017) 14390.
[7] Q. Ding, Y. Zhang, X. Chen, X. Fu, D. Chen, S. Chen, L. Gu, F. Wei, H. Bei, Y. Gao, M. Wen, J. Li, Z. Zhang, T. Zhu, R.O. Ritchie, Q. Yu, Nature 574 (2019) 223–227.
[8] Q.J. Li, H. Sheng, E. Ma, Nat. Commun. 10 (2019) 3563.
[9] R. Zhang, S. Zhao, J. Ding, Y. Chong, T. Jia, C. Ophus, M. Asta, R.O. Ritchie, A.M. Minor, Nature 581 (2020) 283–287.
[10] M. Zhang, Q. Yu, C. Frey, F. Walsh, M.I. Payne, P. Kumar, D. Liu, T.M. Pollock, M.D. Asta, R.O. Ritchie, A.M. Minor, Acta Mater. 241 (2022) 118380.
[11] L. Ding, A. Hilhorst, H. Idrissi, P.J. Jacques, Acta Mater. 234 (2022) 118049.
[12] E. Ma, Scr. Mater. 181 (2020) 127–133.
[13] W.R. Jian, Z. Xie, S. Xu, Y. Su, X. Yao, I.J. Beyerlein, Acta Mater. 199 (2020) 352–369.
[14] Z. Zhang, M.M. Mao, J. Wang, B. Gludovatz, Z. Zhang, S.X. Mao, E.P. George, Q. Yu, R.O. Ritchie, Nat. Commun. 6 (2015) 10143.
[15] F.H. Cao, Y.J. Wang, L.H. Dai, Acta Mater. 194 (2020) 283–294.
[16] T. Cai, Z.J. Zhang, P. Zhang, J.B. Yang, Z.F. Zhang, J. Appl. Phys. 116 (2014) 163512.
[17] Y.T. Zhu, X.Z. Liao, X.L. Wu, Prog. Mater. Sci. 57 (2012) 1–62.
[18] S. Ogata, J. Li, S. Yip, Phys. Rev. B 71 (2005) 224102.
[19] E.B. Tadmor, S. Hai, J. Mech. Phys. Solids 51 (2003) 765–793.
[20] D. Hua, Q. Xia, W. Wang, Q. Zhou, S. Li, D. Qian, J. Shi, H. Wang, Int. J. Plast. 142 (2021) 102997.
[21] Z. Xie, W.R. Jian, S. Xu, I.J. Beyerlein, X. Zhang, Z. Wang, X. Yao, Acta Mater. 221 (2021) 117380.
[22] S.I. Rao, C. Woodward, T.A. Parthasarathy, O. Senkov, Acta Mater. 134 (2017) 188–194.
[23] X.D. Xu, P. Liu, Z. Tang, A. Hirata, S.X. Song, T.G. Nieh, P.K. Liaw, C.T. Liu, M.W. Chen, Acta Mater. 144 (2018) 107–115.
[24] T.M. Smith, M.S. Hooshmand, B.D. Esser, F. Otto, D.W. McComb, E.P. George, M. Ghazisaeidi, M.J. Mills, Acta Mater. 110 (2016) 352–363.
[25] Y. Chen, D. Chen, X. An, Y. Zhang, Z. Zhou, S. Lu, P. Munroe, S. Zhang, X. Liao, T. Zhu, Z. Xie, Acta Mater. 215 (2021) 117112.
[26] P. Yu, R. Feng, J. Du, S. Shinzato, J.P. Chou, B. Chen, Y.C. Lo, P.K. Liaw, S. Ogata, A. Hu, Acta Mater. 181 (2019) 491–500.
[27] K. Jiang, B. Gan, J. Li, Q. Dou, T. Suo, Mater. Sci. Eng. A 816 (2021) 141298.
[28] M. Heczko, V. Mazanova, C.E. Slone, M. Shih, E.P. George, M. Ghazisaeidi, J. Polak, M.J. Mills, Scr. Mater. 202 (2021) 113985.
[29] X. Wu, M. Yang, P. Jiang, C. Wang, L. Zhou, F. Yuan, E. Ma, Scr. Mater. 178 (2020) 452–456.
[30] J. Miao, C.E. Slone, T.M. Smith, C. Niu, H. Bei, M. Ghazisaeidi, G.M. Pharr, M.J. Mills, Acta Mater. 132 (2017) 35–48.
[31] N. Bernstein, E.B. Tadmor, Phys. Rev. B 69 (2004) 094116.
[32] T.J. Balk, K.J. Hemker, Philos. Mag. 81 (2001) 1507–1531.
[33] J.H. Seo, Y. Yoo, N.Y. Park, S.W. Yoon, H. Lee, S. Han, S.W. Lee, T.Y. Seong, S.C. Lee, K.B. Lee, P.R. Cha, H.S. Park, B. Kim, J.P. Ahn, Nano Lett. 11 (2011) 3499–3502.
[34] N.Y. Park, H.S. Nam, P.R. Cha, S.C. Lee, Nano Res. 8 (2014) 941–947.
[35] R. Rezaei, C. Deng, Acta Mater. 132 (2017) 49–56.
[36] J.H. Seo, H.S. Park, Y. Yoo, T.Y. Seong, J. Li, J.P. Ahn, B. Kim, I.S. Choi, Nano Lett. 13 (2013) 5112–5116.
[37] S. Yin, G. Cheng, G. Richter, H. Gao, Y. Zhu, ACS Nano 13 (2019) 9082–9090.
[38] B. Uzer, S. Picak, J. Liu, T. Jozaghi, D. Canadinc, I. Karaman, Y.I. Chumlyakov, I. Kireeva, Mater. Res. Lett. 6 (2018) 442–449.
[39] Q. Ding, X. Fu, D. Chen, H. Bei, B. Gludovatz, J. Li, Z. Zhang, E.P. George, Q. Yu, T. Zhu, R.O. Ritchie, Mater. Today 25 (2019) 21–27.
[40] M. Yang, L. Zhou, C. Wang, P. Jiang, F. Yuan, E. Ma, X. Wu, Scr. Mater. 172 (2019) 66–71.
[41] F. Otto, A. Dlouhy, C. Somsen, H. Bei, G. Eggeler, E.P. George, Acta Mater. 61 (2013) 5743–5755.
[42] G. Laplanche, A. Kostka, O.M. Horst, G. Eggeler, E.P. George, Acta Mater. 118 (2016) 152–163.
[43] S.H. Joo, H. Kato, M.J. Jang, J. Moon, C.W. Tsai, J.W. Yeh, H.S. Kim, Mater. Sci. Eng. A 689 (2017) 122–133.

[44] S.J. Sun, Y.Z. Tian, H.R. Lin, H.J. Yang, X.G. Dong, Y.H. Wang, Z.F. Zhang, Mater. Sci. Eng. A 712 (2018) 603–607.
[45] S.W. Wu, G. Wang, J. Yi, Y.D. Jia, I. Hussain, Q.J. Zhai, P.K. Liaw, Mater. Res. Lett. 5 (2016) 276–283.
[46] S.F. Liu, Y. Wu, H.T. Wang, J.Y. He, J.B. Liu, C.X. Chen, X.J. Liu, H. Wang, Z.P. Lu, Intermetallics 93 (2018) 269–273.
[47] Y. Yue, P. Liu, Q. Deng, E. Ma, Z. Zhang, X. Han, Nano Lett. 12 (2012) 4045–4049.
[48] Z.J. Wang, Q.J. Li, Y. Li, L.C. Huang, L. Lu, M. Dao, J. Li, E. Ma, S. Suresh, Z.W. Shan, Nat. Commun. 8 (2017) 1108.
[49] H.W. Sheng, M.J. Kramer, A. Cadien, T. Fujita, M.W. Chen, Phys. Rev. B 83 (2011) 134118.
[50] P. Yu, J.P. Du, S. Shinzato, F.S. Meng, S. Ogata, Acta Mater. 224 (2022) 117504.
[51] D.M. Dimiduk, C. Woodward, R. LeSar, M.D. Uchic, Science 312 (2006) 1188–1190.
[52] K.S. Ng, A.H.W. Ngan, Acta Mater. 56 (2008) 1712–1720.
[53] Z.J. Wang, Q.J. Li, Z.W. Shan, J. Li, J. Sun, E. Ma, Appl. Phys. Lett. 100 (2012) 071906.
[54] J. Liu, C. Chen, Y. Xu, S. Wu, G. Wang, H. Wang, Y. Fang, L. Meng, Scr. Mater. 137 (2017) 9–12.
[55] H. Li, H. Zong, S. Li, S. Jin, Y. Chen, M.J. Cabral, B. Chen, Q. Huang, Y. Chen, Y. Ren, K. Yu, S. Han, X. Ding, G. Sha, J. Lian, X. Liao, E. Ma, J. Sun, Nature 604 (2022) 273–279.
[56] Y. Yue, P. Liu, Z. Zhang, X. Han, E. Ma, Nano Lett. 11 (2011) 3151–3155.
[57] S. Lee, J. Im, Y. Yoo, E. Bitzek, D. Kiener, G. Richter, B. Kim, S.H. Oh, Nat. Commun. 5 (2014) 3033.
[58] J. Ding, Q. Yu, M. Asta, R.O. Ritchie, Proc. Natl. Acad. Sci. U. S. A. 115 (2018) 8919–8924.
[59] Y.H. Zhang, Y. Zhuang, A. Hu, J.J. Kai, C.T. Liu, Scr. Mater. 130 (2017) 96–99.
[60] S. Zhao, Y. Osetsky, G.M. Stocks, Y. Zhang, npj Comput. Mater. 5 (2019) 13.
[61] M. Shih, J. Miao, M. Mills, M. Ghazisaeidi, Nat. Commun. 12 (2021) 3590.
[62] T.Z. Khan, T. Kirk, G. Vazquez, P. Singh, A.V. Smirnov, D.D. Johnson, K. Youssef, R. Arróyave, Acta Mater. 224 (2022) 117472.
[63] C.R. LaRosa, M. Ghazisaeidi, Acta Mater. 238 (2022) 118165.
[64] L. Liu, J. Wang, S.K. Gong, S.X. Mao, Phys. Rev. Lett. 106 (2011) 175504.